

# Development of a Fully Instrumented, Resonant Tensegrity Strut

MER 498 – Report

03/13/2017

Student: Kentaro Barhydt

Advisor: Professor William Keat

*I affirm that I have carried out all academic endeavors with full academic honesty*

X\_\_\_\_\_

## Contents

Introduction & Background .....	1
Theoretical Models of a Single Tensegrity Strut .....	6
Implementation of Inertial Measurement Unit on Tensegrity Strut .....	15
Design and Implementation of a Low-Frequency Vibration Motor .....	21
Conclusions .....	31
References .....	32
Appendices .....	33

## Introduction & Background

A tensegrity is a structure composed of purely compressive members (struts) held in equilibrium by tensile elements (springs). The springs and struts act in synergy with each other in that the compression in the struts keep the structure from collapsing into itself while the tension in the springs hold the struts in their upright position (Fig.1). This project will focus on the development of an active modular tensegrity strut capable of actuating its resonant frequencies and capturing its dynamics using onboard motion tracking instrumentation. The vibration of the strut will also be modeled to gain a theoretical understanding of its dynamic behavior.

The term “tensegrity”, coined by Buckminster Fuller, is a portmanteau of the two words: tensile, and integrity, which describes its ability to maintain mechanical stability through its natural tendency to disperse stresses throughout its entire body [1]. This is possible because the dynamic coupling between nodes (ends of struts where springs are connected) allow for a continuous compliance in tension distance between nodes, meaning it can deform to virtually any shape without changing its topology and will return to its original geometry when all external forces are removed. The robust compliance of tensegrity structures make them attractive in the



Fig.1 – 6-bar tensegrity

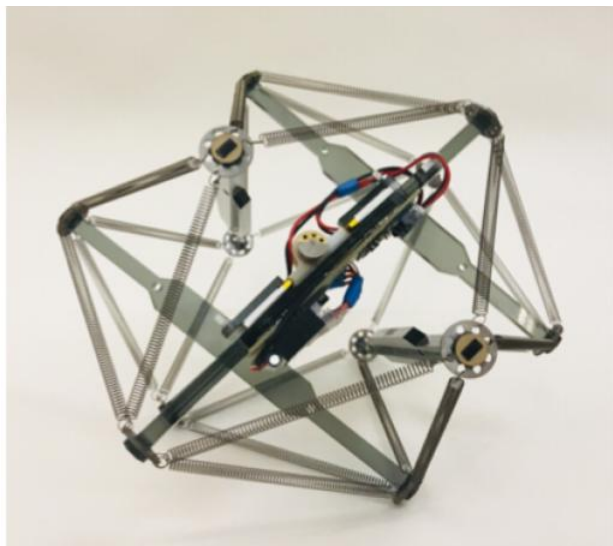


Fig.2 – Vibrating tensegrity robot

field of soft robotics. The spring connections between struts absorb external forces and disperse stress throughout its body, giving them a high strength-to-weight ratio and making them resilient against impact forces that would cause traditional rigid robots to break. Tensegrities can adjust the prestresses in its tensile connections as well, allowing it to deform under its own weight and comply to different terrains. For these reasons, the NASA Ames Research Center is currently developing a tensegrity-based robotic platform for planetary exploration, called SUPERball [2]. The current prototype locomotes by shifting its center of mass to achieve a rolling gait, which is controlled by adjusting the prestress in its individual tensile connections. Its tensegrity-based structure allows its gait to mechanically comply to different surfaces, making its ability to traverse variable terrains more robust than previous planetary explorers. The high impact resistance also enables high speed entry and landing without the use of airbags [3].

In addition to compliance, the deformation capabilities of tensegrity structures allow for a greater range of complex dynamic motion than rigid structures. The dynamic coupling between struts also allows for simplified actuation of complex motions that would otherwise require multiple actuators using a rigid structure design. These characteristics parallel the robust complexity of biomechanical locomotive systems found in animals and have caused tensegrities to gain interest in the field of bioinspired robotics. Thomas Bliss *et al.* developed autonomous control of a tensegrity-based swimmer that mimics a fishtail using Central Pattern Generators (CPGs), which are systems of neurons found to control rhythmic motion responsible for locomotion in animals, to achieve closed-loop entrainment to desired swimming gaits [4]. The BEST Lab at University of California, Berkeley, has also developed a quadruped that utilizes a tetrahedral tensegrity structure as a spine to support complex motions between the robot's front and rear legs, allowing for greater efficiency and stability in traversing irregular terrains [5].

Research at Union College lead by Professor John Rieffel has focused specifically on exploiting the nonlinear complex dynamics of tensegrity structures. The tensegrities used are designed to locomote through the vibration of the struts, which is evolved to achieve optimal locomotion and control using genetic algorithms. These algorithms are based on the concept of morphological communication. In, “Morphological Communication: Exploiting Coupled Dynamics in a Complex Mechanical Structure to Achieve Locomotion”, Rieffel et al. presents morphological communication as phenomena commonly found in nature in which dynamically coupled physical systems act as neural networks capable of transferring signals through nodes that can simultaneously actuate and sense other nodes [6]. This applies to the evolutionary process in that the individual active (vibrating) struts are able to individually adapt their driving frequency without direct communication with any of the other struts so that the gait of the entire tensegrity structure evolves as a whole. The struts only have knowledge of their own dynamics, and the forces applied by the springs affect those dynamics and act as feedback for the strut to adjust to. This reduces the necessary computation significantly, allowing the tensegrity to bypass the processing limitations of controlling its nonlinear coupled dynamics and take advantage of its compliant properties and wide range of motion patterns.

Complex dynamic coupling is typically avoided in engineering design due to this inability to control it through traditional means. Additionally, dynamic coupling is also typically avoided to prevent resonance from occurring. This is because it can cause uncontrollable increases in vibrational magnitude, which can be harmful to a rigid system’s operation and structure. As a part of exploiting nonlinear dynamic coupling, Rieffel’s research hypothesizes that optimal locomotion in vibrating tensegrities is achieved when driven at its resonant frequencies due to the conservation of vibrational energy that causes the increase in amplitude.

This extends the implication that the natural frequencies, if known, should be utilized when finding optimal gaits. The current version of the genetic algorithms only tracks the net motion of the entire tensegrity robot and does not observe the dynamics of individual struts, making the evolutionary process inefficient in that it cannot guide its genotype selection towards dynamic behaviors known to correlate with optimal locomotion. Implementing methods of artificial selection based on individual strut dynamics would significantly increase the efficiency of evolution, therefore increasing the tensegrity's ability to quickly adapt to variable environments.

Previous research has explored the dynamic response of tensegrity structures under forced vibration. Oppenheim and Williams have demonstrated that the natural geometric flexibility of tensegrities at equilibrium reduces the effect of natural damping in the tensile elements, causing a longer rate of amplitude retention [7]. Bel Hadj Ali and Smith demonstrated vibration control of a fixed, five-module tensegrity vertically actuated at one fixed node, and determined that natural frequencies can be shifted away from excitation by adjusting prestress levels [8]. Bohm and Zimmermann developed a symmetrical, single-actuated vibrating tensegrity robot that could control the speed and direction of locomotion by adjusting prestress and driving frequency respectively [9]. Bliss *et al.* developed and experimentally validated closed-loop resonance entrainment of a linearly constrained biomimetic tensegrity swimmer to optimal locomotive gaits using linear oscillators for cable actuation [10].

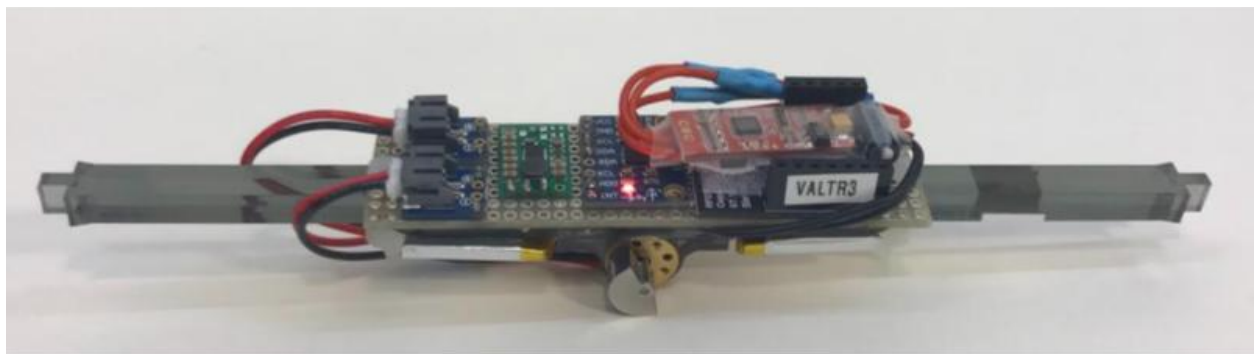


Fig.3 – Wireless modular strut for tensegrity robot

This project follows those of Union College graduates Alexander Chu (ME '17) and Riley Konsella (CPE '17), whose senior projects (partially and fully respectively) aimed to develop a modular vibrating strut for a new wireless version of the tensegrity [11][12]. The first prototype of the wireless tensegrity strut (Fig.3) was completed afterward by Kentaro Barhydt (ME '18) during a summer research fellowship. This project will utilize this wireless tensegrity prototype for experimentation and make modifications and/or additions to its design where necessary. In addition to developing a modular strut, Chu's project aimed to fabricate an irregular 15-bar tensegrity robot using topology determined using Professor William Keat's form-finding algorithm. This algorithm takes defined properties of the tensegrity as parameters and deduces its topology at its lowest energy state, its vibrational mode, and its natural frequency [12]. Using this algorithm, the topology of a tensegrity resulting in specific natural frequencies can be deduced.

The goal of this project is to develop a modular strut capable of actuating and capturing these resonant modes so that their relationship to optimal locomotion can be determined. Achieving this will allow for further work in testing Rieffel's hypothesis and experimental validation of theoretical models developed in characterizing resonance.

## 2. Theoretical Models of a Single Tensegrity Strut

To properly characterize the dynamics of a multi-strut vibrating tensegrity, the dynamics of a single strut must first be understood. Analyzing the behavior of an isolated strut provides the insight necessary to analytically interpret experimental observations of the full tensegrity. Therefore, the dynamics of an isolated single strut were first modeled using analytical and numerical methods. In order to validate Keat's small-angle linearity assumption used in the predictive natural frequency algorithm, both a linear and nonlinear model were developed to observe possible differences in their results given the same parameters. Having a computational model also allowed for extensive parameter analysis, providing insight into how different geometric constants and input variables affect the natural frequency of the strut.

### 2.1 Nonlinear Model

The nonlinear models for single strut vibration were derived based on the experimental setup in which the strut vibration would be isolated, as seen in Figure 4. The model is nonlinear simply as a result of the system. The setup included a total of eight springs with four on attached

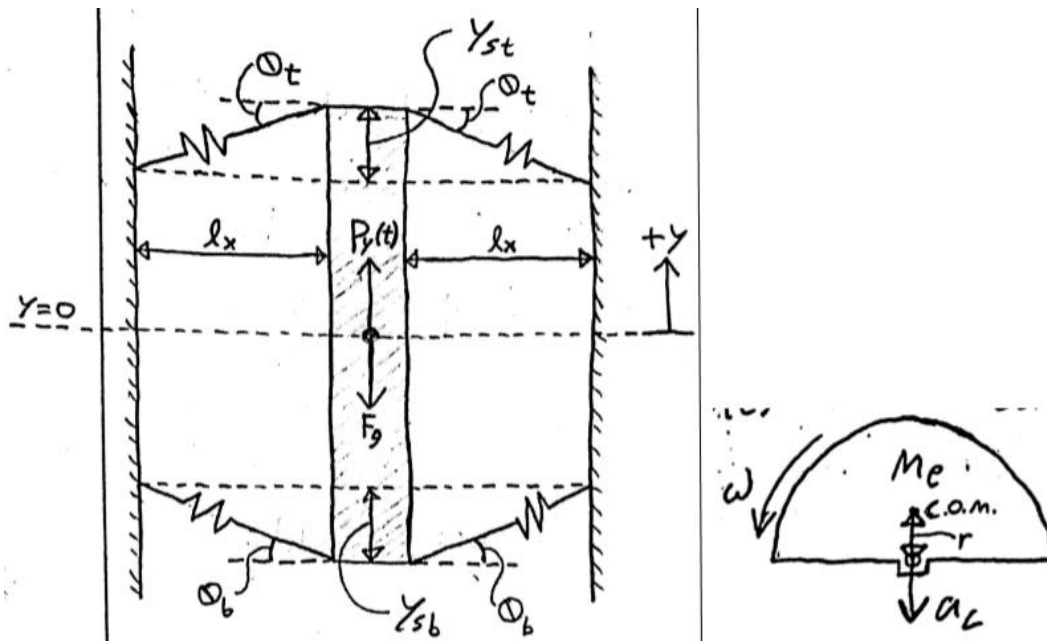


Fig.4 – Force diagram of single strut in test configuration (left) and eccentric weight of vibration motor



to each end. Only the vertical displacement was observed and motion in other dimensions were considered negligible because the strut movement along its axis was assumed to be dominant in the particular tensegrity structure that the isolated spring geometry is based on. The lack of actuation in the horizontal plane also implies that the spring configuration stays symmetric along the axis of the strut at any given time, meaning the length and angle each spring is always equal to all other springs connected to the same strut end. The motor speed was assumed to be constant, as the electronic user input given to the tensegrity robot should translate directly through to the mechanical input of the motor. If the voltage input and motor function do not have a constant and direct relation, then experiments that rely on controlling frequency parameters, like the genetic algorithm experiments conducted at Union College, could not properly characterize the frequency response of the tensegrity as the input function would be accurately represented. Since tensegrity structures are assumed to have negligible damping, the theoretical models initially do not account for potential damping forces. The nonlinear model was first derived as a second order differential equation as a function of time  $t$  with state variables of vertical displacement  $y$  and acceleration  $\ddot{y}$ :

$$\ddot{y} = -\frac{4}{M_s}(y + h_0) \left( k - \frac{kl_0 - F_0}{\sqrt{l_x^2 + (y + h_0)^2}} \right) - \frac{4}{M_s}(y - h_0) \left( k - \frac{kl_0 - F_0}{\sqrt{l_x^2 + (y - h_0)^2}} \right) + \frac{1}{M_s}P_y(t) - g \quad (1)$$

where  $P_y(t)$  denotes the vertical component of the centripetal force input of the motor:

$$P_y(t) = M_e r \omega^2 \sin(\omega t) \quad (2)$$

The first and second terms of the equation denote the top and bottom sets of springs respectively.

The variables and constants of both the nonlinear and linear equations are defined as:

$$t = \text{time (s)}$$

$y$  = Vertical displacement of strut from  $y=0$  (m)  
 $y_s$  = Vertical distance between end of strut and respective spring mounting points (m)  
 $h_o = |y_s|@ y=0$  (m)  
 $\theta$  = Angle of spring from horizontal (rad)  
 $l_x$  = Spring length @  $\theta=0^\circ$  (rad)  
 $l_o$  = Free length of spring (m)  
 $g$  = Acceleration of gravity ( $\text{m/s}^2$ )  
 $F_y$  = Vertical component of spring tension (N)  
 $F_o$  = Initial tension in springs (N)  
 $M_s$  = Mass of strut (Kg)  
 $M_e$  = Mass of eccentric weight (Kg)  
 $r$  = Centroidal radius of eccentric weight (m)  
 $\omega$  = Motor speed (rad/s)

The strut displacement is solved for though Runge-Kutta state propagation using MATLAB (App. A). Both models were run at a sampling rate of 10,000 Hz and set the parameters of the strut properties similarly to that of the physical strut currently in use. The model output the overall strut displacement, velocity, and acceleration over time, as seen in Figure 5.

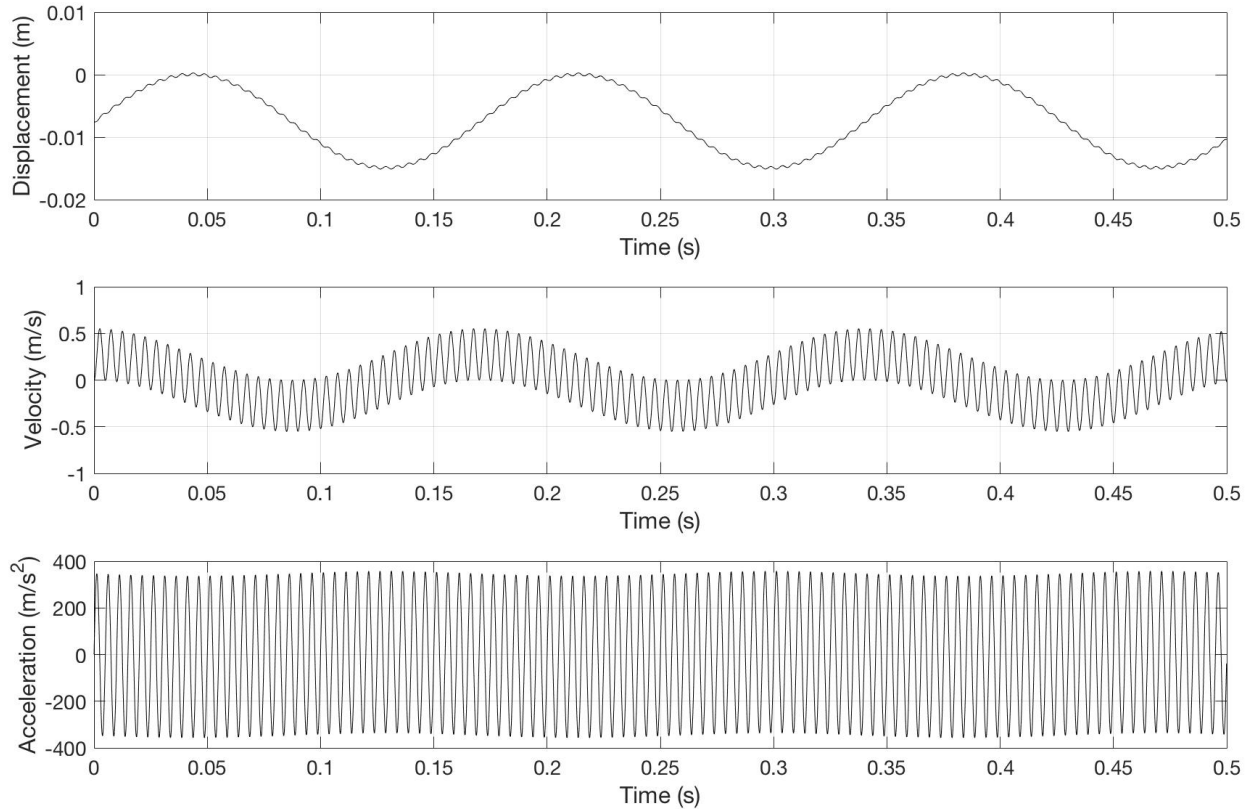


Fig.5 – Displacement, velocity, and acceleration of single strut over time

## 2.2 Linear Model

The linear model was derived based on the same experimental setup used for the nonlinear model with the exception that the assumption that the change in spring angle is small enough to consider negligible, as seen in figure 6.

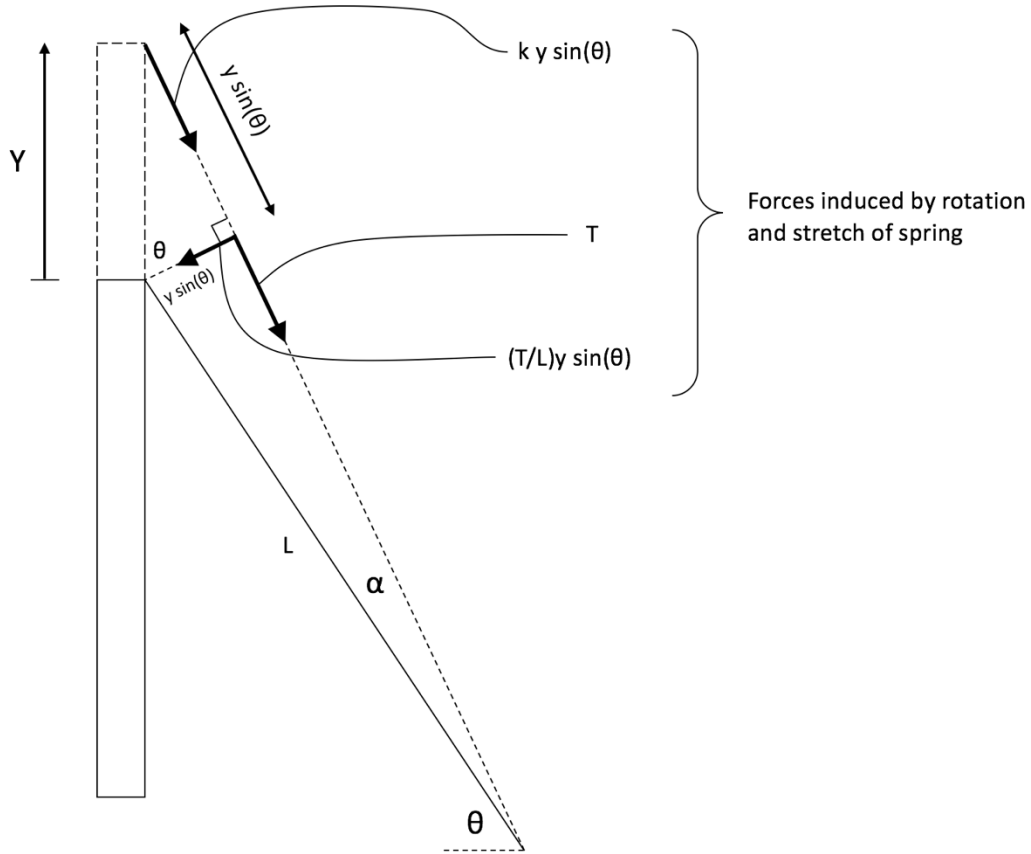


Fig.6 – Spring tension diagram of single spring for linear model. Small angle assumption assumes distance  $Y$  is small enough to assume angle  $\alpha$  is negligible.  $\theta$  is constant.

This assumption resulted in the following equation for acceleration:

$$\ddot{y} = -\frac{8}{M_s} \left( k \sin^2 \theta - \frac{T}{\sqrt{l_x^2 + h_0^2}} \cos^2 \theta \right) y + \frac{1}{M_s} P_y(t) - g \quad (3)$$

where  $T$  denotes the tension in the springs when  $y = 0$ :

$$T = k \left( \sqrt{l_x^2 + h_0^2} - l_0 \right) + F_0 \quad (4)$$

The spring constant term (multiple of  $y$ ) could then be determined from this equation since  $\theta$  is constant, making the entire term constant:

$$\Sigma k = k \sin^2 \theta - \frac{T}{\sqrt{l_x^2 + h_0^2}} \cos^2 \theta \quad (5)$$

This was then used to derive the natural frequency of the system, resulting in:

$$f_n = \frac{1}{2\pi} \sqrt{\frac{\Sigma k}{M_s}} = \frac{1}{2\pi} \sqrt{\frac{k \sin^2 \theta - \frac{T}{\sqrt{l_x^2 + h_0^2}} \cos^2 \theta}{M_s}} \quad (6)$$

### 2.3 Results

The nonlinear and linear models generated fundamentally equal results and therefore validated the small angle displacement assumption.

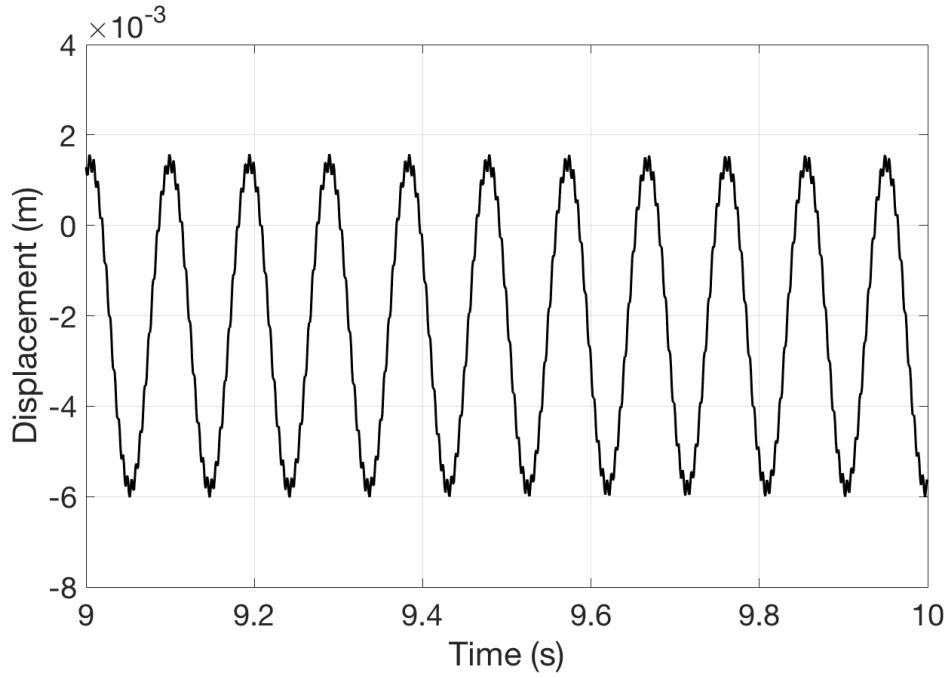


Fig.7 – Nonlinear model: vertical displacement of strut over time

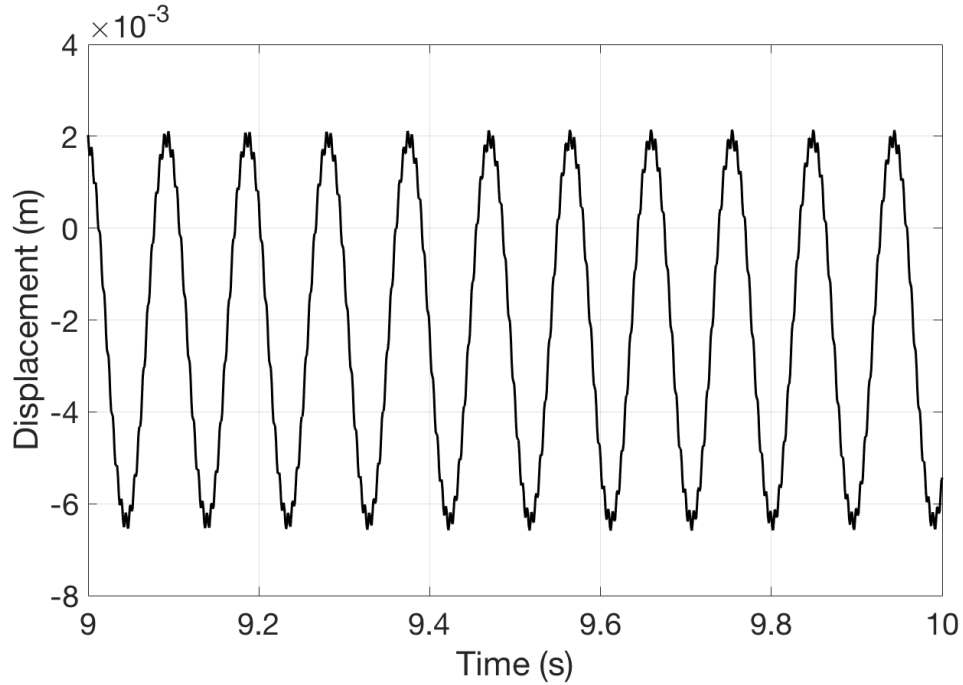


Fig.8 – Linear model: vertical displacement of strut over time

As shown in figure 7 and 8, the function and periods of the frequency responses for both models aligned with each other. Both plots reveal one overarching and one underlying sine wave with frequencies of 10.6 Hz and 200 Hz respectively. The amplitude of the linear model is slightly larger than that of the nonlinear model and there is an apparent phase shift of approximately 20 degrees between them. However, both these discrepancies can be ignored for the purposes of characterizing the strut dynamics because the function for both models are the same and change proportionally as input frequency is adjusted. The frequency is crucial in that it must stay consistently equal between the two models in order for the small angle displacement to be valid. The frequency for both the nonlinear and linear responses aligned, therefore theoretically confirming the assumption. A Fast Fourier Transform (FFT) was performed on the numerical displacement results of the linear model, which confirmed the existence of two sine waves and their respective frequencies (Fig. 9).

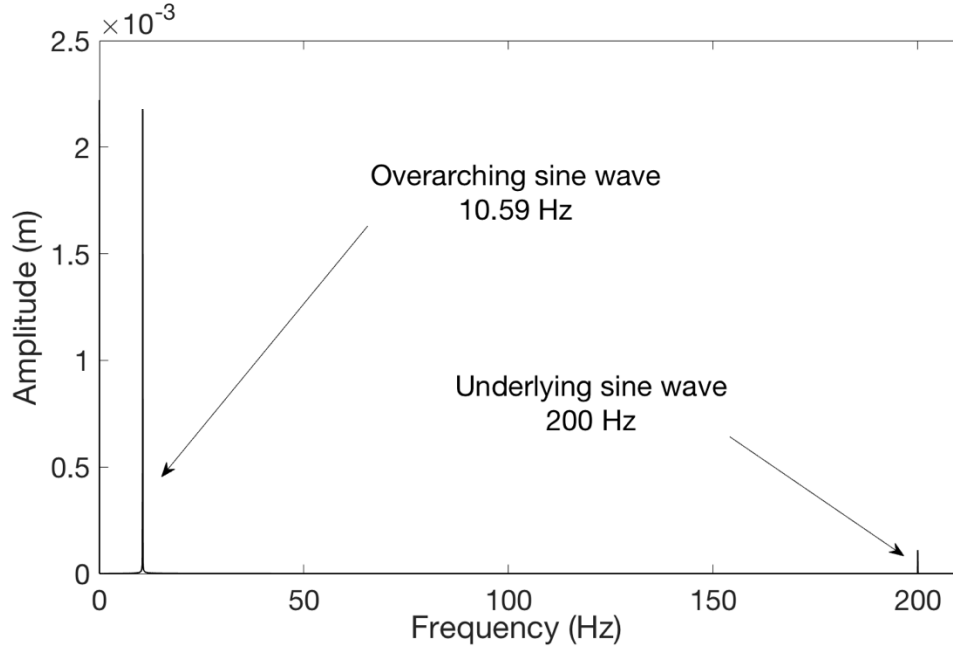


Fig. 10 – Fast Fourier Transform of linear displacement results

The natural frequency was calculated using (6) resulting in  $f_n = 10.93$  Hz, which aligned with the overarching sine wave frequency found in both models with an error of 3.1%. When tested at different motor speeds, the numerical and analytical natural frequency results stay within a 3.5% to 4.5 % range of error with each other. While the significance of this error to predicting natural frequencies will need to be determined experimentally, it is small and consistent enough to conclude that the overarching sine wave present in the model results represents the system's natural frequency. The FFT also revealed a second sine wave with a smaller amplitude than that of the overarching sine wave and a frequency of 200 Hz. This frequency matched the driving frequency of the vibration motor and stayed within a  $\pm 0.005\%$  margin of error when tested at different motor speed inputs. From this correlation, it can be concluded that the underlying sine wave present in the model results represents the driving frequency of the strut. The identification of both the sine waves that comprise the vibration response in context to the physical system theoretically confirms the validity of the linear model

in describing the strut dynamics. This in turn validates the use of the small angle displacement assumption in Keat's natural frequency algorithm.

A parameter analysis was conducted on the linear model to determine the limit and magnitude of impact each independent parameter of the natural frequency equation (6). The ranges of values analyzed for each parameter were estimated based on their reasonable upper and/or lower limits for the current tensegrity design.

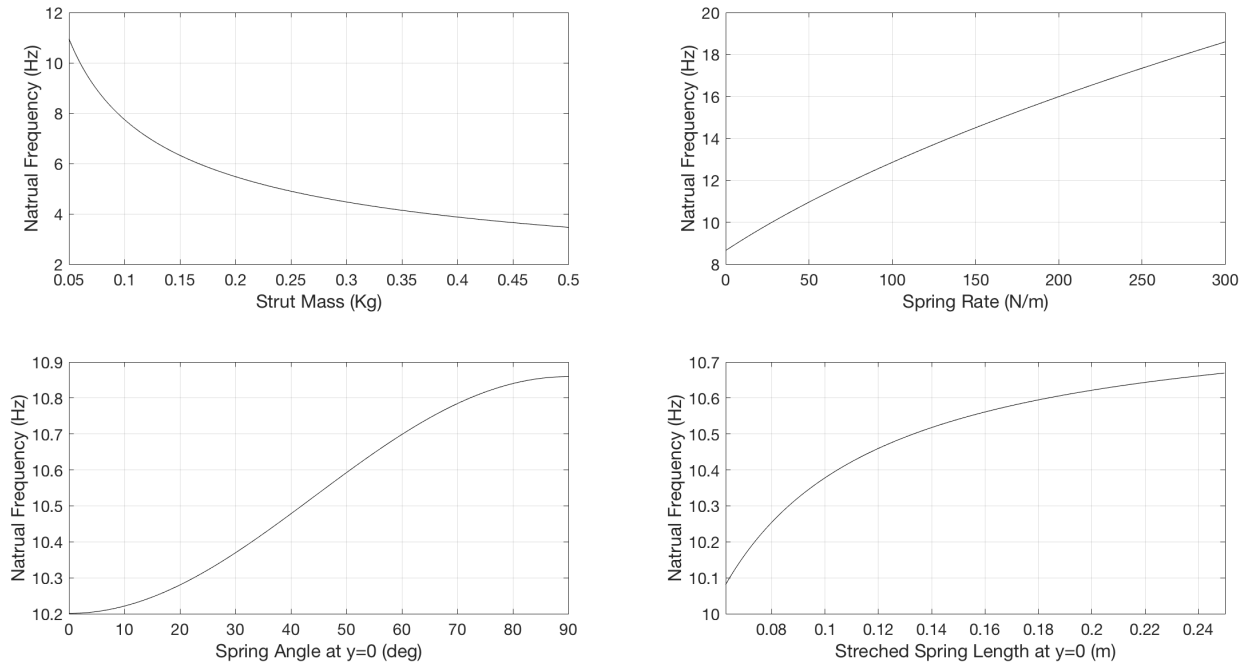


Fig.11 – Natural frequency vs. strut mass, spring rate, spring angle at  $y = 0$ , and stretched spring length at  $y = 0$

As seen in figure 11, the mass of the strut and the spring rate have the greatest impact on natural frequency, although that impact diminishes logarithmically as their values increase. Spring rate was shown to have the most consistent (although actually a root function) relationship with natural frequency for the given range. The spring angle and stretched length at  $y = 0$  were both relatively inconsequential to the natural frequency.

## 2.4 Conclusions

The small-angle displacement assumption used in Keat's predictive natural frequency

algorithm was successfully validated by developing and comparing linear and nonlinear models of single strut vibration. Both models represent underlying frequencies of isolated strut motion that aligned with the experimental setup as well. The mass of the strut and spring rate were also determined to have a significant impact on the natural frequency of the system through a parameter analysis, while the spring angle and stretched spring length were observed to be nearly arbitrary.



### **3. Implementation of Inertial Measurement Unit on Tensegrity Strut**

In order to empirically validate the theoretical models and observe phenomena such as resonance, the dynamics of the tensegrity must be experimentally captured. Previous work using the tensegrity for evolutionary algorithm testing only tracked the overall movement of the tensegrity's center of mass across a horizontal plane, which severely limited the understanding of the mechanics behind what caused optimal locomotion. Therefore, the motion of each individual strut must be captured in order to accurately observe its dynamic behavior. Given the constraints of the tensegrity design and application, this must also be achieved while maintaining its wireless control and small size.

#### **3.1 Data Collection and Analysis**

The necessary motion capture was achieved by implementing a 6-axis inertial measurement unit (IMU) onto the strut. This method was chosen for its relatively high accuracy and sampling rate, small size, and low cost. Other methods explored included visual tracking using a high speed camera and spring tension measurement using load cells. Camera tracking is ideal for the tensegrity design since it does not require any modification to the circuitry of the strut. This method had previously been explored by Union College computer science students, who tracked the position of a node (connection point between strut and springs) of the tensegrity over time relative to the frame of the camera. However, this method was ruled out due to the complexity needed to accurately track a tensegrity. Multiple cameras would be needed to track at least six individual struts in three dimensions at a high enough resolution to accurately measure position and a high enough frequency to accurately capture high frequencies (sampling rate must be at least twice the highest frequency being observed). Camera tracking systems are sold commercially explicitly for this purpose, but also cost hundreds of thousands of dollars.

Therefore, due to the complexity of tensegrity dynamics and the lack of equipment, camera tracking was deemed an infeasible approach for this project.

The other method, using spring tension load cells, was also deemed infeasible due to the lack of lightweight load cells available on the market. Since each spring would need at least one load cell equipped to properly instrument the entire tensegrity, a 6-bar tensegrity would need four load cells per strut (24 springs distributed between 6 struts), which would increase the total weight by a very significant amount (lightest load cell found was 3.2 g, meaning 12.8g would be added to the strut which weighs 60 g). The space taken up at the end of the struts would also interfere with collisions with the ground during vibration, and the additional amp needed to operate the cells would occupy even more space in the circuitry. An alternative exists in using conductive rubber cord that changes its resistance as it stretches, allowing for its length to be measured based on the current passing through it given a constant voltage. However, the accuracy of this device does not meet the requirements of the project in that its specifications provide a range of resistance per unit of length, and therefore was also ruled out as the best potential motion capture method.

An IMU was integrated into the strut circuit to allow for onboard motion tracking. The gyro/accelerometer used was a MPU-6050 module that can sense up to  $\pm 16$  g at a resolution of  $\pm 2048$  samples/g with six degrees of freedom: three-axis translation and three-axis rotation. The MPU-6050 weighs  $\sim 1$  g and has a maximum sampling rate of 1000Hz for translational acceleration and 8000 Hz for rotational acceleration. Since oscillating motion must be recorded at a sampling rate at least twice its frequency, the highest translational frequency that can be captured is 500 Hz and the highest rotational acceleration that can be captured is 4000 Hz.

While the IMU is able to sample at 1000 Hz, Bluetooth connection to the strut was

unable to send samples to the user's computer at the same rate. The maximum sampling rate achievable by sending a live feed of samples over Bluetooth was approximately 7 Hz. Attempts were made to increase the rate, such as minimizing the data sent per sample and communicating between two Bluetooth modules instead of directly to the computer, but none could successfully achieve a rate over 60 Hz. The minimum sampling rate requirement is approximately 400 Hz in order to capture the higher frequencies obtainable by the vibration motor. The genetic algorithms test a wide range of frequency inputs, so maintaining this range is important to finding optimal locomotion in full tensegrity structures later in this project.

To increase the sampling rate to an adequate speed, onboard data storage was implemented onto the strut using a microSD card and microSD shield module. This removed the bottleneck of the slow Bluetooth communication and allowed the IMU to send data directly to the microSD card through the microprocessor. The microSD shield connects to the plug-in pins on the RFDuino, so the circuit was revised to avoid connecting other components to the pins occupied by the shield. With this modification, the strut is now able to sample at a rate of 425 Hz, making proper data acquisition of high frequencies possible.

The program that runs the modular strut, written in Arduino (C/C++), also required substantial revisions to allow for high sampling rate capabilities. The original code, written by James Boggs and Riley Konsella, included a manual pulse width modulation (PWM) function that allowed for digital control of the brushless motor speed. This method of motor control needed to be replaced due to its use of a delay function in timing the output pulse, which stopped all processes in the code for the specified amount of time. Since the total pulse period was set to 20 ms, the shortest possible amount of time elapsed between each sample was 20 ms, meaning the sampling rate possible was 50 Hz. This issue was eliminated by programming the motor

control and data sampling to run in parallel instead of in series, which was accomplished in part by the implementation of the updated brushed DC gearmotor (discussed further in section 4). Although the Arduino code runs the modular strut, an interactive external python code is used to control the strut by controlling the behavior of the Arduino code by restarting it and resetting its parameters based on user input. Therefore, because the motor speed does not need to change continuously over a gradient of values, the motor speed user input control was implemented in the python code so that the internal behavior of the Arduino code can assume constant motor speed throughout its runtime. This allowed the PWM function to be initialized and run until the program is terminated, thus removing it from the loop in which data sampling is iteratively run.

### 3.2 Test Apparatus

Capturing the dynamics of a single vibrating strut required a method of isolating strut vibration, so a test rig was designed and built to ground the external mounting points of the strut's spring connections and hold the strut in a symmetrical configuration, as seen in figure 12.

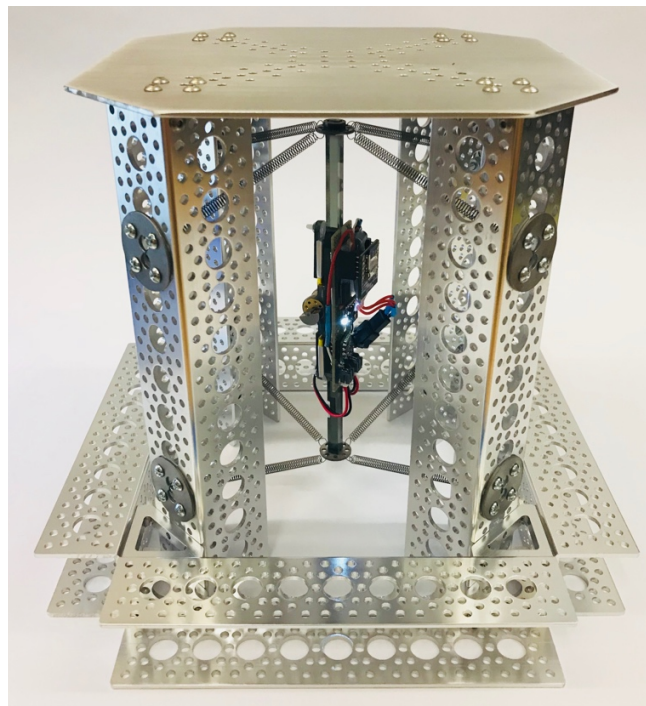


Fig.12 – Test rig with pattern channel structure

The test rig was constructed using aluminum pattern channels and sheet metal. Pattern channels were chosen as the primary structural component of the rig due to their flexural strength and fastening adjustability. The test rig must accommodate single strut experiments in multiple configurations with varying mass and spring geometry parameters, so easy modification of the rig dimensions is important for reusability and efficient testing. The flexural strength of the channels also prevents vibrations in the structure due to the oscillating tension in the springs. Separate spring connection parts were made from sheet metal to allow for different mounting heights on the channels. A problem commonly faced when previously using struts was that fastening springs required its ends to bend open to hook onto the mounting point. Therefore, the spring connection parts made for the test rig were designed with connections thin enough for the springs to attach to without plastically deforming them.

A design manufactured entirely from sheet metal was considered as an alternative to the pattern channel design. The structure would be made from interlocking sheets of 0.09" thick aluminum and welded together. This design would be completely manufacturable at Union College's machine shop, allowing for full control of features like spring mount placement and strut accessibility. However, the pattern channel design was ultimately chosen for its ease of assembly and modification. The sheet metal structure could have been designed with similar fastening features as the pattern channels, but would require additional mounting brackets to do so, which would significantly increase the total cost of the rig. The sheet metal could be bent and fastened to perpendicular surfaces as an alternative to using brackets, but this would add an additional manufacturing step that would take a significant amount of time. This would also decrease the precision of the structure due to the machine shop's limited ability to precisely bend thicker sheets to specified radii.

### **3.4 Conclusions**

Onboard motion tracking for individual struts was implemented into the modular strut design using a IMU, allowing for translational and rotational acceleration measurement sampling in three dimensions. Sampling data was collected onboard using microSD memory cards in order to create a direct communication channel capable of processing high-frequency sampling data. This system can consistently achieve a sampling rate of  $\sim 425$  Hz, and its implementation did not require any significant modifications to the physical design of the modular tensegrity strut. This fast communication was developed alongside the new custom vibration motor, so experimental results of this system are outlined in the following section.

## **4. Design and Implementation of a Low-Frequency Vibration Motor**

The vibrating motor of the modular tensegrity strut needed to be redesigned in order for it to drive the theoretical resonant frequencies of the 6-bar tensegrity as well as the current design of the single strut. Using Keat's model, the natural frequencies of a 6-bar tensegrity composed of the modular tensegrity struts would have a number of resonant frequency combinations between its active struts, all of which fall between 2 Hz and 17.6 Hz. The operating range of the brushless motor from the previous design, 40 Hz to 230 Hz, does not encompass any of these frequencies. Therefore, a custom motor was designed, manufactured, and implemented onto the strut to achieve a lower frequency range that can actuate resonant frequencies, as well as increase overall amplitude.

### **4.1 Vibration Motor Design**

A gearmotor was chosen for the new motor design because the mechanical advantage of the gearbox accomplished the exact purpose of the design renewal: given the same power input, the gear motor increased the torque and decreased the rotational speed of the output shaft. The inclusion of a gearbox was necessary since nearly all the motors researched either had too high of a minimum driving frequency or too low of a stall torque. Achieving these results through mechanical advantage instead of an alternative electronic design was necessary because the power input could not increase without significantly increasing the weight of the strut and requiring a redesigned battery mounting system.

The Pololu 10:1 Micro Metal Gearmotor LP 6V was chosen for the vibration motor design for its operating frequency range of 0 Hz to 21.7 Hz. Although the maximum motor speed is rated at free-run, the load torque resistance was assumed to be negligible compared to the difference in the highest possible motor and resonant frequencies since the torque input is only

needed at high speeds to maintain the eccentric weight's constant speed. Its rated voltage of 6V is still lower than the 7.4V supply provided by the modular strut's two LiPo batteries, making it readily compatible with the current power configuration. The Pololu micro-gearmotor product line also includes motor fastening accessories, meaning the motor can now be attached and detached from the strut, unlike the previous friction-fit adhesive mount for the brushless motor.

Another crucial benefit of this specific motor was that it has a D-shaft output, meaning attachments can be easily fastened and unfastened to and from it. This is important because a custom eccentric mass was needed to reach the desired high vibrational amplitude at the low resonant frequencies. The final eccentric weight design aimed to concentrate its mass as far from the axis of rotation as possible, as seen in figure 13.



Fig.13 – Pololu 10:1 Micro Metal Gearmotor LP 6V equipped with custom eccentric weight

The weight was cut from a 5/16" thick 4140 hardened steel bar using a waterjet cutter and tapped for a 3M set screw. The weight was cut in the "cut-off semicircle" shape, as seen in figure 14, in order to maximize the eccentric radius while maintaining the same weight and thickness. This was done in order to maximize centripetal force while avoiding any increase in the overall



weight of the strut or outer radius of the weight. This shape was selected from a group of experimental shapes, as seen in Appendix B.

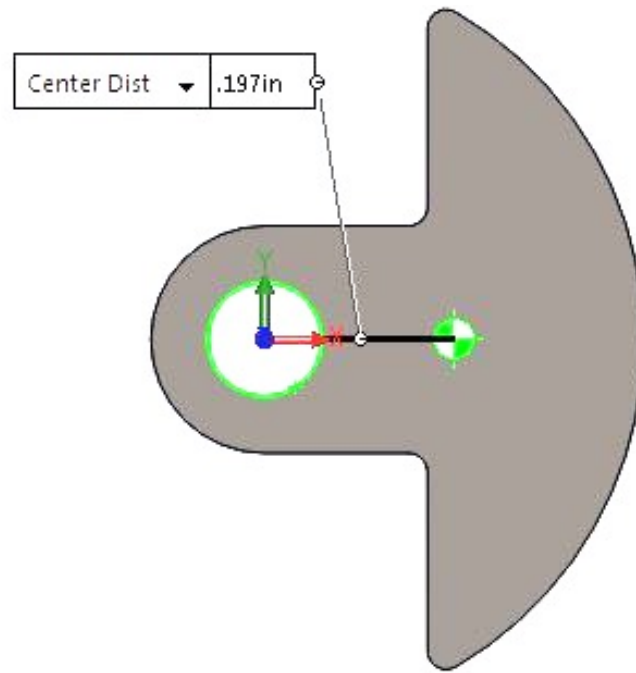


Fig. 14 – Eccentric weight cross-sectional shape and eccentric radius

The eccentric weight is fastened to the motor using thread-locking set screws to allow for modularity if the weight parameters of the strut vibration need to be changed for different experiments. Due to the eccentric weight and the stall torque of the gearmotor, the minimum speed at which the motor could run at an input value of 17 (1.44 Hz nominal).

## 4.2 Electronics Design

Since brushless vibration DC motor was replaced with a brushed DC gearmotor, the electronic component of the motor control system needed to be modified. The brushless electronic speed controller (ESC) was replaced with the Pololu DRV8838 Single Brushed DC Motor Driver Carrier in order to control the gearmotor using PWM. The motor driver acts as a power amplifier in that it receives an external PWM signal, amplifies it using a voltage source, and outputs the signal proportional to the voltage source to the DC motor. An additional 6V step-

down voltage regulator was implemented to provide a constant 6V voltage supply to the motor driver in order to avoid scaling inconsistencies when sending motor speed PWM signals. The final circuit of the modular strut is shown in figure 15.

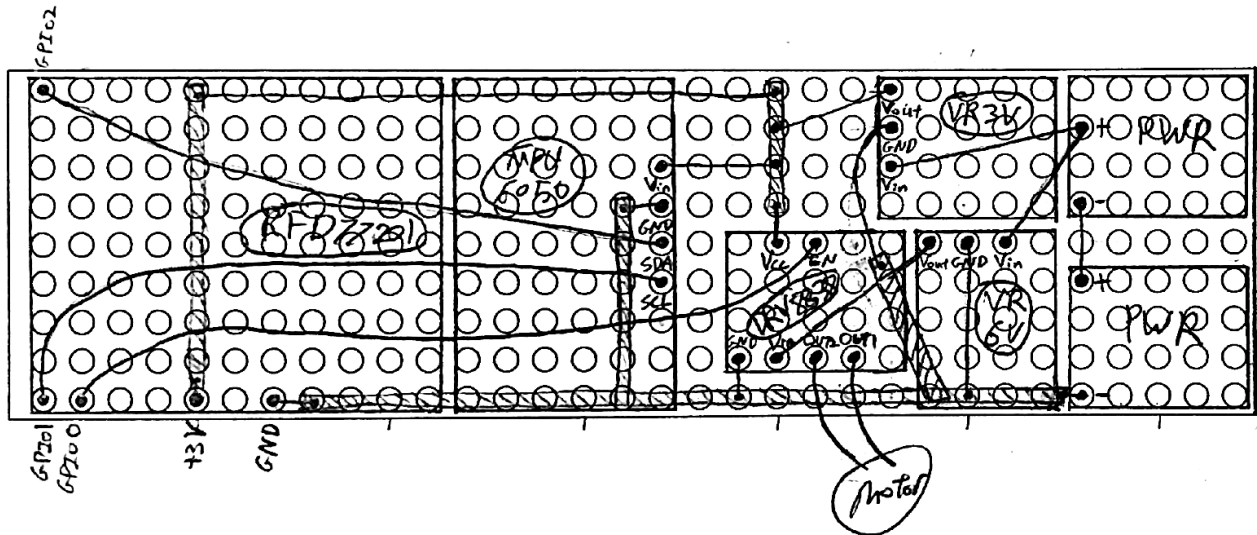


Fig.15 – Hand-drawn schematic of modular strut circuit and protoboard layout. Lines connecting dots denote wire connections, and long rectangles with hatching marks denote copper tape.

With the electronic design updates and complete, the IMU motion capture system and custom brushed gearmotor were integrated with the physical strut to make the latest version of the fully instrumented, resonant tensegrity strut, as seen in figure 16.

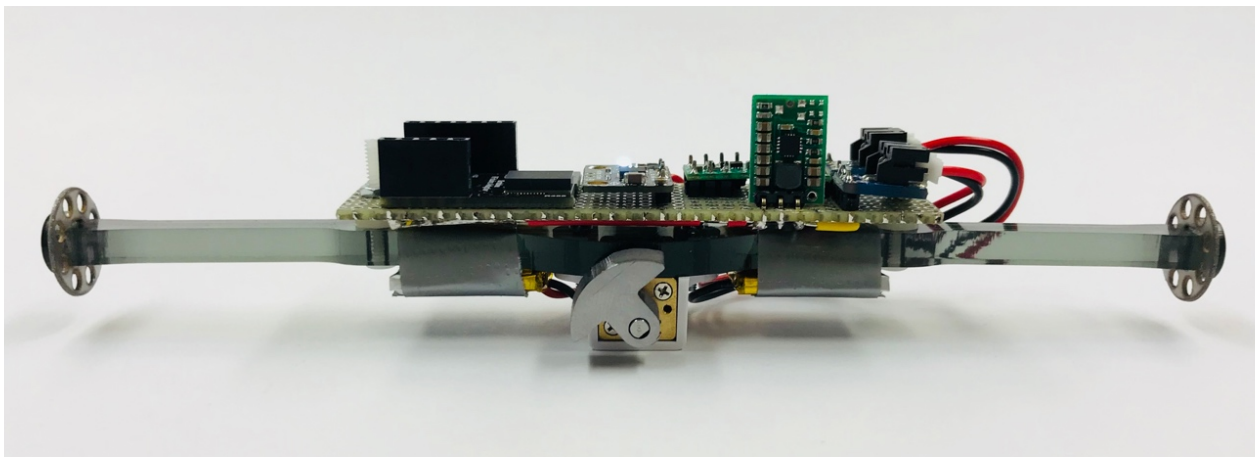


Fig.16 – Latest prototype of fully instrumented, resonant tensegrity strut. Vertical chip is 3.3V step-up/step-down regulator used in previous design and is vertical due to lack of space on protoboard. Final prototype of strut will use smaller 3.3V step-down regulator that will fit flat on protoboard. Batteries will also be secured in place using clips, similar to that of previous design, instead of using duct tape as shown in the picture.

### 4.3 Experimental Excitation of Single Strut Resonant Frequency

A series of tests were performed in which the instrumented strut was run at every frequency input possible. These tests were run on a single strut using the pattern channel test rig. The strut's onboard Arduino code is programmed to take all two-digit hexadecimal values, meaning it can take all numbers between 0 and 255. The tests were actually run starting at 15 and ending on 249, meaning a total of 235 tests were run. These values convert to PWM output in that a 0 input means the pulse is 100% off and the motor is stationary, and a 255 input means the pulse is 100% on and the motor is at its fastest speed. A python code was written to run the strut at a given speed for 30 seconds and then turn it off for another 30 seconds. This process would be repeated for every frequency input between the user-defined upper and lower limits, with each test increasing the input by one. The motion capture data from the IMU was appended to the microSD card data file after each test.

The first attempt at running these tests failed due to the unexpectedly high amplitude the strut vibrated at when excited at its resonant frequency. To accommodate for this, longer channels were bought and a higher test rig was constructed. The two 150 mAh batteries lasted throughout the entire testing session. The IMU collected a total of approximately 2.96 million samples, which accumulated into a 48.6 Mb ASCII file. This size was too large for either MATLAB or Excel to process without returning an error or crashing, so a script was written that reads and separates this data into individual files for each test (App.A.5).

Before discussing the results of the tests, it should be noted that the theoretical models were rendered partially inaccurate due to an invalid assumption. In their current state, the theoretical models fail to account for continuous changes in motor speed due to the acceleration it experiences from the vibration of the strut. This was determined to be significant as a result of

observing an unexpected phenomenon in the strut's steady state vibration while testing, in that when actuated near the system's natural frequency, the oscillations of the motor and strut would create a mode-locked loop and converge at the natural frequency. While this demonstrates an interesting phenomenon that will be explored in future work, it also shows that the voltage input from the user does not directly translate to the motor speed of the tensegrity strut. Since this phenomenon is most likely due to the force of the strut acting on the eccentric weight, which changes throughout its period, the motor speed cannot be assumed to be constant throughout its period as well. Therefore, the function of the motor must be modeled as well for the theoretical models to accurately characterize the entire system.

Despite this, the accuracy of the onboard motion capture system was confirmed and resonance was still observed in the tensegrity strut. The experimental frequency response for each test was observed and compared against high-speed video footage to confirm that the frequency and amplitude align. The IMU is mounted on the strut so that the x-axis of its local orientation is parallel to the rotational axis of the vibration motor, and the y-axis is parallel to the axis along the length of the strut. The experimental frequency response of the strut when run at an input value of 134 (nominal frequency  $\sim 11.4$  Hz) is shown in figure 17. Frequency locking can be observed in this test through the change in frequency and amplitude. Between  $t=0$ s and  $t=10$ s, the vibration is observed to have an approximate frequency of  $\sim 12$  Hz and an amplitude of  $\pm 1$  g, whereas once the vibration approaches steady state between  $t=27$ s and  $t=30$ s, the vibration was observed to have an approximate frequency of  $\sim 9$  Hz and an amplitude of  $\pm 16$  g. These results were compared against high-speed camera footage recorded at 240 FPS, as seen in figure 18.

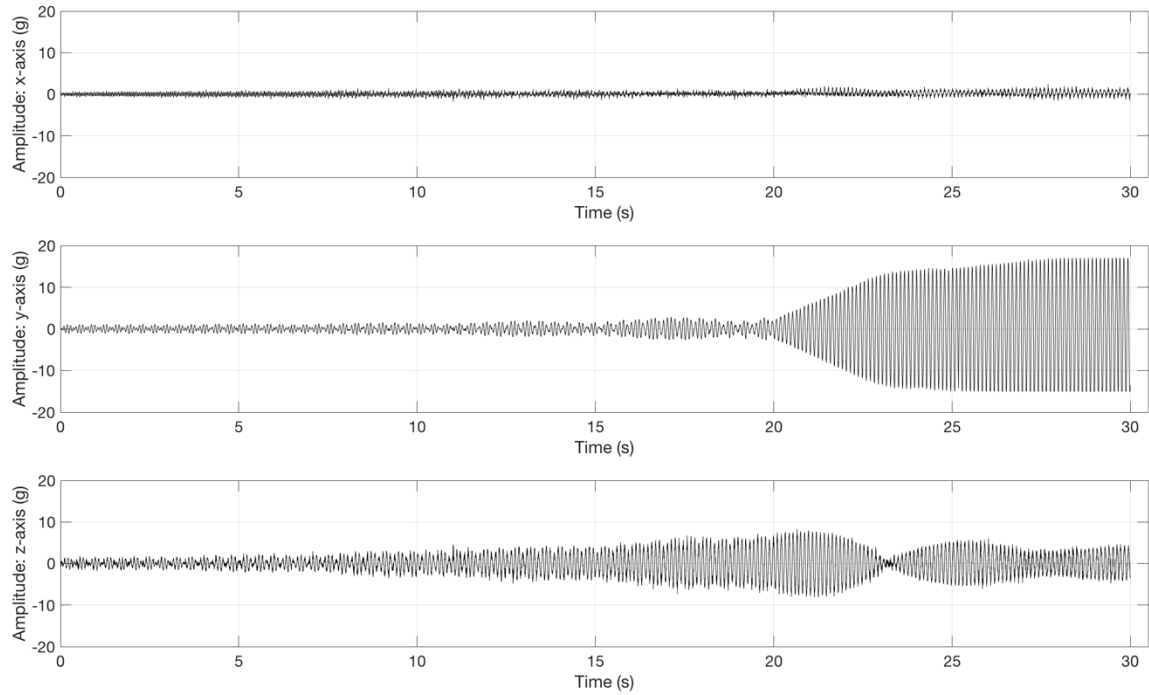


Fig.17 – Experimental acceleration data of single strut vibration with input value of 134 (~11.4 Hz nominal)

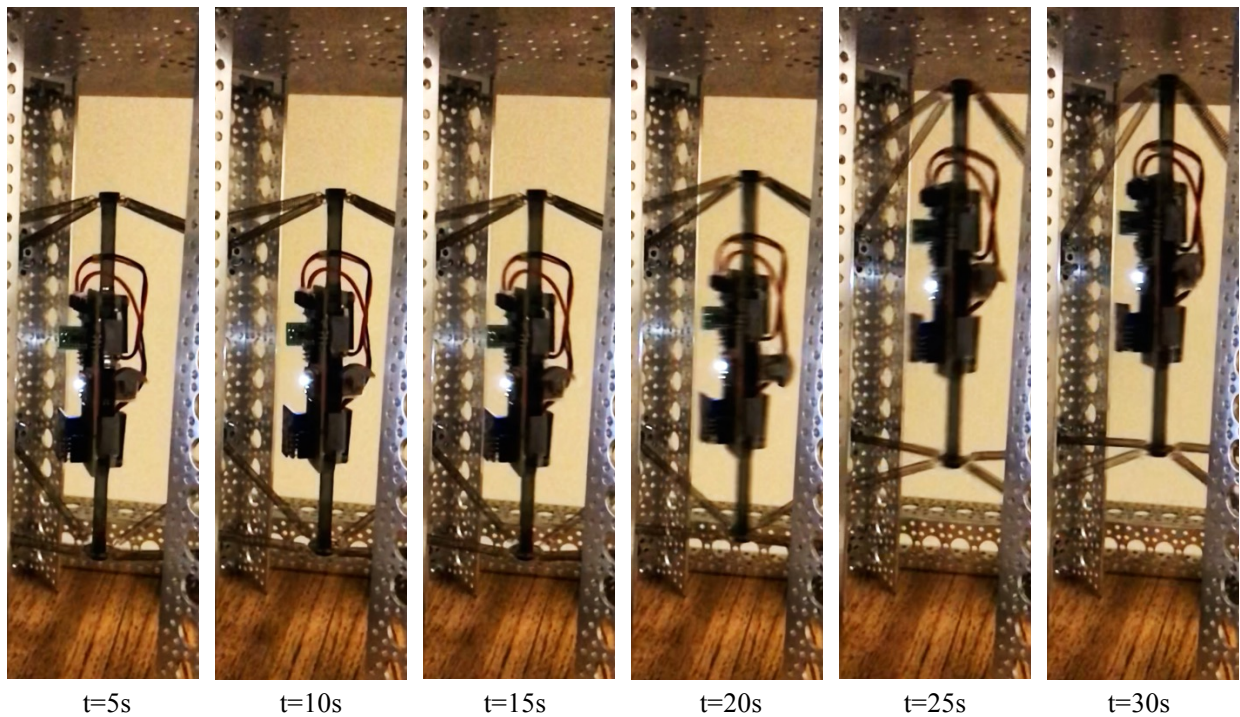


Fig.18 – Still frames from high-speed camera footage of vibrating tensegrity strut with input value of 134 (~11.4 Hz nominal). Each still frame shows strut at peak amplitude along the y-axis during a period closest to a time interval of 5 seconds.

While the high speed footage was used to validate the overall behavior of the frequency response, the precise acceleration measurement could not be confirmed due to a lack of scale in the video. However, the resonance could still be observed without exact measurements of acceleration, as the peaks in amplitude were observed on a scale relative to that of the other frequency inputs. The experimental frequency measurement was confirmed by counting the number of oscillations the strut experienced between a 5 second time interval when the strut vibration was in steady state. This was then compared to the number of oscillations observed in the measured data from the IMU.

The full frequency response of the strut vibration is visualized in figure 19. The amplitude was measured from the steady state vibration of each test (App.A.6). From this frequency response, the resonant frequency appears to lie between the input values 110 and 140. However, due to the Frequency locking phenomenon, the resonant frequency most likely does not lie

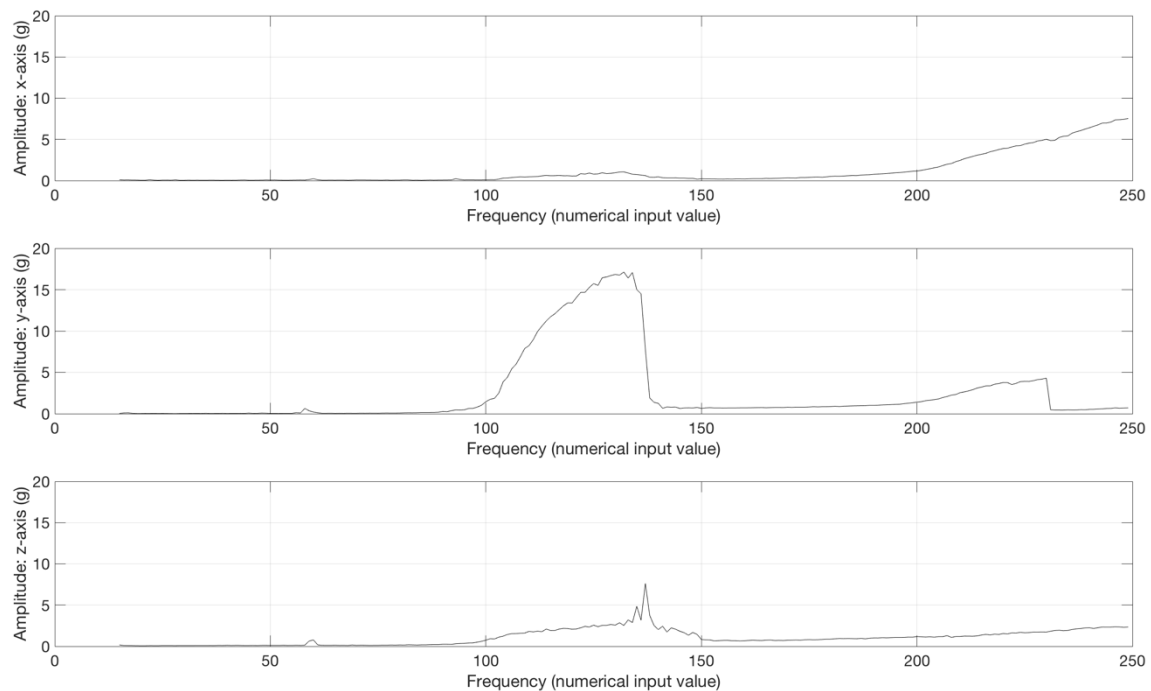


Fig.19 – Experimental frequency response of single strut vibration. Frequency domain is plotted as input

values for motor speed control due to indirect relationship between motor frequency and motor input voltage.

at the actual peak of this plot. The actual peak was observed to lie at input value 117 with an amplitude of 12.5 g and a nominal frequency of 9.94 Hz. This was determined by observing at what value the vibration began to experience frequency locking. As seen in figure 20, the highest input value used before frequency locking begins is 117.

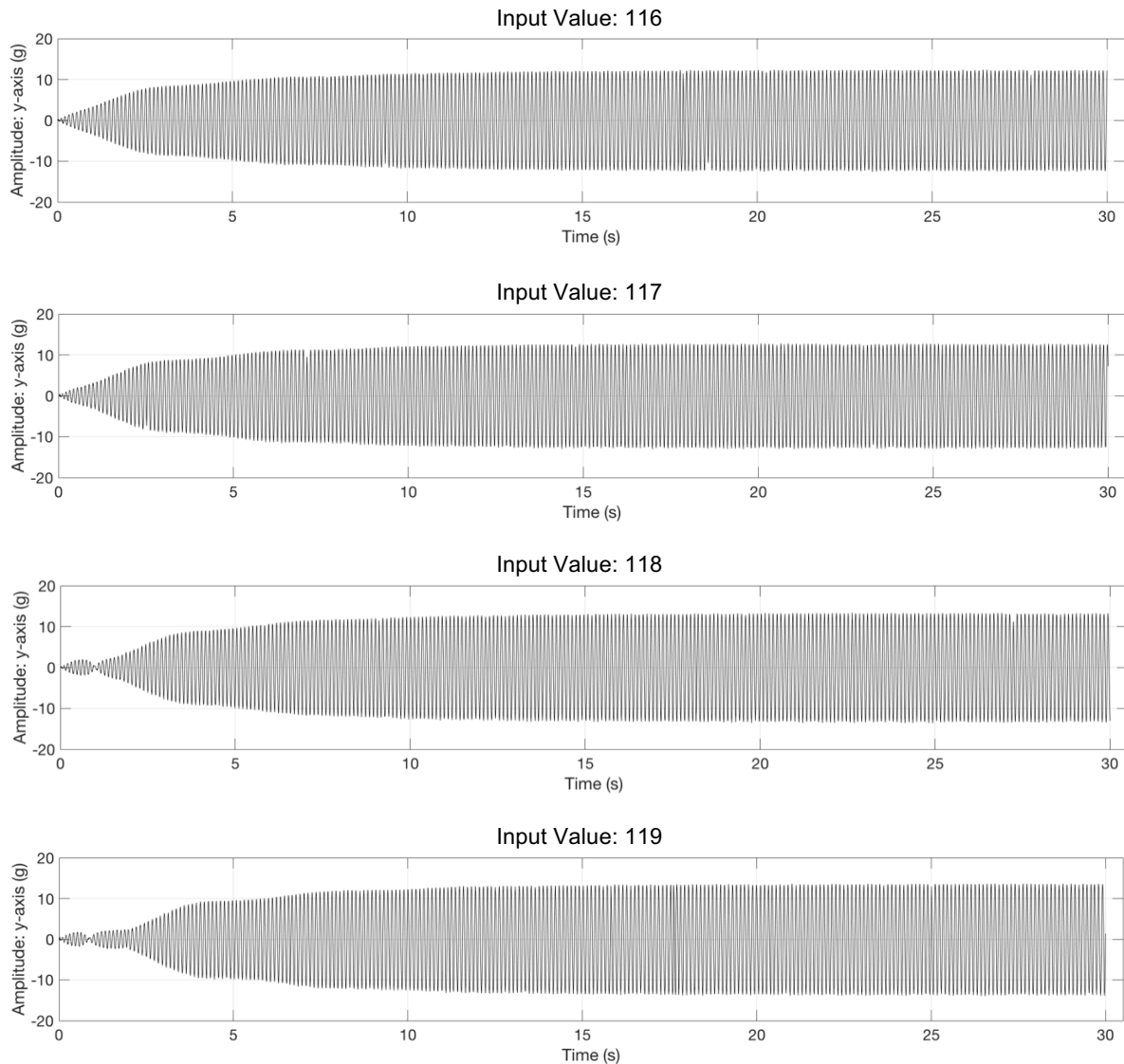


Fig.20 – Y-axis experimental acceleration data for input values 116, 117, 118, and 119.

A FFT was performed on the y-axis experimental data for input value 117 to determine

the experimental underlying frequency of the steady state strut vibration, as seen in figure 21.

The experimental resonant frequency was observed to be 9.67 Hz. When compared to the

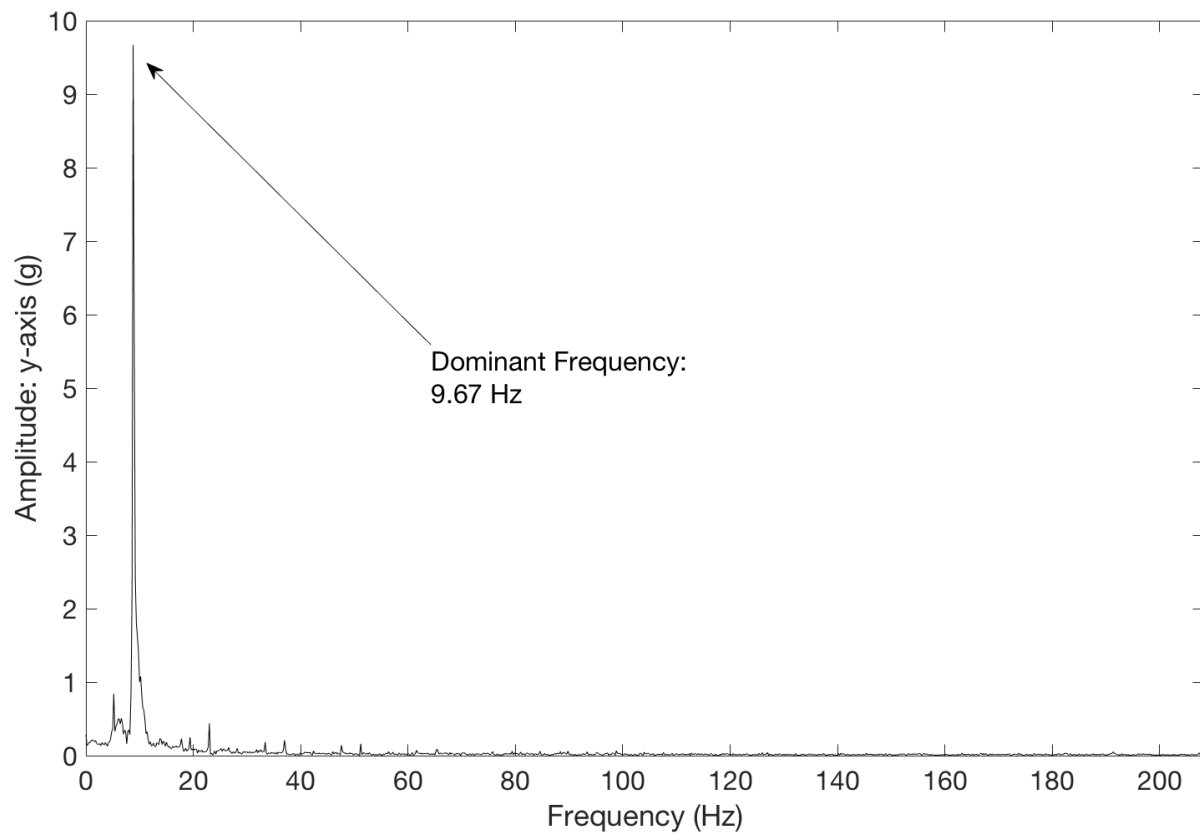


Fig.19 – Experimental frequency response of single strut vibration. Frequency domain is plotted as input values for motor speed control due to indirect relationship between motor frequency and motor input voltage.

frequency observed using the linear model (10.93 Hz), the theoretically natural frequency has a calculated error of 13.03%.



## 5. Conclusions

The modular active wireless strut has been fully instrumented for onboard motion tracking data collection and modified to actuate its resonant frequencies. Onboard acceleration measurement with a sampling rate of 425 Hz was implemented using a 6-axis IMU. The acceleration data was stored onboard as well using a microSD card. A custom vibration motor was designed and manufactured using a brushed DC motor and a waterjet cut eccentric weight to actuate the natural frequencies of the strut. The custom vibration motor has an operating range of 1.44 Hz to 21.7 Hz and can vibrate the strut at amplitudes of up to  $\pm 16$  g.

Future work will focus on modifying the theoretical models to accommodate for frequency locking. This will primarily involve modeling the motor speed as a function of the strut acceleration as a feedback loop. Accounting for this will not only improve the accuracy of the models but will also allow for a better understanding of how the coupled dynamics between struts affect the vibration of struts individually. Further testing will also need to be conducted to characterize the error of the linear and nonlinear models and the experimental range of in which the IMU can properly capture amplitude and frequency.

## References

- [1] Ingber, Donald E. . “The Architecture of Life .” *Scientific American* Jan 1998: 48-57.
- [2] A. P. Sabelhaus, J. Bruce, K. Caluwaerts, P. Manovi, R. F. Firoozi, S. Dobi, A. M. Agogino, and V. Sunspiral, “System design and locomotion of SUPERball, an untethered tensegrity robot,” 2015 IEEE International Conference on Robotics and Automation (ICRA), Jul. 2015.
- [3] J. Bruce, K. Caluwaerts, A. Iscen, A. P. Sabelhaus, and V. Sunspiral, “Design and evolution of a modular tensegrity robot platform,” 2014 IEEE International Conference on Robotics and Automation (ICRA), Sep. 2014.
- [4] T. Bliss, T. Iwasaki, and H. Bart-Smith, “Central Pattern Generator Control of a Tensegrity Swimmer,” *IEEE/ASME Transactions on Mechatronics*, vol. 18, no. 2, pp. 586–597, 2013.
- [5] A. P. Sabelhaus, H. Ji, P. Hylton, Y. Madaan, C. Yang, A. M. Agogino, J. Friesen, and V. Sunspiral, “Mechanism Design and Simulation of the ULTRA Spine: A Tensegrity Robot,” Volume 5A: 39th Mechanisms and Robotics Conference, 2015.
- [6] Rieffel, J. , Valero-Cuevas, F. and Lipson, H. (2010) "Morphological Communication: Exploiting Coupled Dynamics in a Complex Mechanical Structure to Achieve Locomotion". *J. R. Soc. Interface*.
- [7] I. J. Oppenheim, “Vibration of an Elastic Tensegrity Structure,” *European Journal of Mechanics*, vol. 20, 2001.
- [8] N. Bel Hadj Ali, “Dynamic Behavior and Vibration Control of a Tensegrity Structure,” *International Journal of Solids and Structures*, vol. 47, no. 9, pp. 1285–1296, 2010.
- [9] V. Bohm and K. Zimmermann, “Vibration-driven mobile robots based on single actuated tensegrity structures,” 2013 IEEE International Conference on Robotics and Automation, 2013.
- [10] T. Bliss, J. Werly, T. Iwasaki, and H. Bart-Smith, “Experimental Validation of Robust Resonance Entrainment for CPG-Controlled Tensegrity Structures,” *IEEE Transactions on Control Systems Technology*, vol. 21, no. 3, pp. 666–678, Mar. 2012.
- [11] R. Konsella, “Designing a Modular Strut for Union’s Tensegrity Robot,” thesis, 2017.
- [12] A. Chu, “Through Yonder Window Breaks: The Rise of JULIET,” thesis, 2017
- [13] J. Rieffel, W. Keat, B. Humphreys, M. Khazanov. “Exploiting Dynamical Complexity in A Physical Tensegrity Robot to Achieve Locomotion.” *Advances in Artificial Life* 12 (2013)

## Appendix A.1: Vibration Model MATLAB Code – Nonlinear

### StrutVibrationModelNonlinear.m

```
% Single VVValtr Strut Vibration
% Linear Model

clear all

global g Me Ms r omega k l0 lx F0 h0
g = 9.81; % m/s^2
Me = 0.005; % kg
Ms = 0.056; % kg
r = 4 * 0.0058 / (3 * pi()); % m
omega = 2 * pi() * 5000 / 60; %rad/s
k = 0.19 * 175.196945; % N/m
l0 = 2.47 * 0.0254; % m
lx = 3 * 0.0254; % m
F0 = 0.4 * 4.45; % N
h0 = 0.05; % m

% Define time step and sampling range
deltat = 0.001; % s
startTime = 0; % s
endTime = 100; % s
t = [startTime:deltat:endTime];

% Calculate Ysag
Ysag = findYsag();

% Initialize state vector
yInit = [Ysag;0];
y = yInit;

% Conduct state propogation using Runge Kutta method
for i = 1:length(t)-1
    ydot(:,i) = accelerationFunction(y(:,i),t(i));
    k1 = ydot(:,i);
    k2 = accelerationFunction(y(:,i) + (deltat/2)*k1,t(i));
    k3 = accelerationFunction(y(:,i) + (deltat/2)*k2,t(i));
    k4 = accelerationFunction(y(:,i) + deltat*k3,t(i));
    y(:,i+1) = y(:,i) + (deltat/6)*(k1 + 2*k2 + 2*k3 + k4);
end

Yfft = fft(y(1,:));
Yfft_mag = abs(Yfft)/length(Yfft);

% Calculate state derivative at last time sample
ydot(:,length(t)) = accelerationFunction(y(:,length(t)-1),t(i));

% Plot displacement
figure('name','Nonlinear Model - Displacement','units',...
    'normalized','position',[0,0.5,0.5,0.5])
plot(t,y(1,:), 'k', 'LineWidth', 1.5)
set(gca, 'FontSize', 20)
set(gca, 'YTick', (-1:0.002:1))
xlabel('Time (s)', 'FontSize', 22)
```

```

ylabel('Displacement (m)','FontSize',22)
xlim([max(0,endTime-1),endTime])
ylim([-0.014,0.004])
grid on

% Plot FFT results
binDomain = 1:length(Yfft_mag);
freqDomain = binDomain*(1/endTime);
figure('name','Magnitude vs Frequency FFT results - Linear','units',...
    'normalized','position',[0.5,0.5,0.5,0.5])
plot(freqDomain,Yfft_mag)
xlabel('bins','FontSize',22)
ylabel('Amplitude','FontSize',22)
xlim([0,freqDomain(end)/2])
set(gca, 'FontSize', 20)

% Plot velocity
figure('name','Velocity of Cart Along Surface Over Time','units',...
    'normalized','position',[0,0,1,1])
plot(t,y(2,:))
set(gca, 'FontSize', 14)
xlabel('Time (s)','FontSize',16)
ylabel('Velocity (m/s)','FontSize',16)
grid on

% Plot acceleration
figure('name','Acceleration of Cart Along Surface Over Time','units',...
    'normalized','position',[0,0,1,1])
plot(t,ydot(2,:))
set(gca, 'FontSize', 14)
xlabel('Time (s)','FontSize',16)
ylabel('Acceleration (m/s^2)','FontSize',16)
grid on

% Plot displacement, velocity, and acceleration together
figure('name','Displacement, Velocity, and Acceleration Over Time',...
    'units','normalized','position',[0,0,1,1])
subplot(3,1,1)
plot(t,y(1,:))
set(gca, 'FontSize', 14)
xlabel('Time (s)','FontSize',16)
ylabel('Displacement (m)','FontSize',16)
grid on
subplot(3,1,2)
plot(t,y(2,:))
set(gca, 'FontSize', 14)
xlabel('Time (s)','FontSize',16)
ylabel('Velocity (m/s)','FontSize',16)
grid on
subplot(3,1,3)
plot(t,ydot(2,:))
set(gca, 'FontSize', 14)
xlabel('Time (s)','FontSize',16)
ylabel('Acceleration (m/s^2)','FontSize',16)
grid on

```

## accelerationFunction.m

```
function ydot = accelerationFunction(y,t)

global g Me Ms r omega k l0 lx F0 h0

ydot1 = y(2);
ydot2 = -(4/Ms)*(y(1)+h0)*(k-((k*l0-F0)/sqrt(lx^2+(y(1)+h0)^2)))...
        -(4/Ms)*(y(1)-h0)*(k-((k*l0-F0)/sqrt(lx^2+(y(1)-h0)^2)))...
        -g+(Me/Ms)*r*omega^2*sin(omega*t);

ydot = [ydot1;ydot2];

end
```

## findYsag.m

```
function ysag = findYsag()

global g Ms k l0 lx F0 h0

lmax = l0 + 3.200;
ymax = sqrt(lmax^2 - lx^2) - h0;

for y = -ymax:0.0000001:ymax
    Fsum = -4*(y+h0)*(k-((k*l0-F0)/sqrt(lx^2+(y+h0)^2)))-4*(y-h0)*...
            (k-((k*l0-F0)/sqrt(lx^2+(y-h0)^2)));
    sum = Fsum-Ms*g;
    if sum <= 0.0001 && sum >= -0.0001
        ysag = y;
    %         disp(sum);
    %         disp(y)
end
end

end
```

## Appendix A.2: Vibration Model MATLAB Code – Linear

### StrutVibrationModelLinear.m

```
% Single VVValtr Strut Vibration
% Linear Model

clear all

global g Me Ms r omega k l0 lx F0 h0 ysag L T theta
g = 9.81; % m/s^2
Me = 0.005; % kg
Ms = 0.056; % kg
r = 4 * 0.0058 / (3 * pi()); % m
omega = 2 * pi() * 12000 / 60; %rad/s
k = 0.19 * 175.196945; % N/m
l0 = 2.47 * 0.0254; % m
lx = 3 * 0.0254; % m
F0 = 0.4 * 4.45; % N
h0 = 0.05; % m
ysag = findYsag(); % m
L=(lx^2+h0^2)^0.5;
T=k*(L - l0) + F0;
theta=atand(h0/lx);

% Define time step and sampling range
deltat = 0.001; % s
startTime = 0; % s
endTime = 100; % s
t = [startTime:deltat:endTime];

% Initialize state vector
y2Init = [0;0];
y2 = y2Init;

% Conduct state propogation using Runge Kutta method
for j = 1:length(t)-1
    y2dot(:,j) = accelerationFunction_v5(y2(:,j),t(j));
    k1 = y2dot(:,j);
    k2 = accelerationFunction_v5(y2(:,j) + (deltat/2)*k1,t(j));
    k3 = accelerationFunction_v5(y2(:,j) + (deltat/2)*k2,t(j));
    k4 = accelerationFunction_v5(y2(:,j) + deltat*k3,t(j));
    y2(:,j+1) = y2(:,j) + (deltat/6)*(k1 + 2*k2 + 2*k3 + k4);
end

% Calculate state derivative at last time sample
y2dot(:,length(t)) = accelerationFunction_v5(y2(:,length(t)-1),t(j));

% Fast Fourier Transform
Yfft = fft(y2(1,:));
Yfft_mag = abs(Yfft)/length(Yfft);

% Plot displacement2
figure('name','Linear Model - Displacement','units',...
    'normalized','position',[0,0,0.5,0.5])
plot(t,y2(1,:), 'k', 'LineWidth', 1.5)
set(gca, 'FontSize', 20)
```

```

set(gca, 'YTick', (-1:0.002:1))
xlabel('Time (s)', 'FontSize', 22)
ylabel('Displacement (m)', 'FontSize', 22)
xlim([max(0, endTime-1), endTime])
ylim([-0.014, 0.004])
grid on

% Plot FFT results
binDomain = 1:length(Yfft_mag);
freqDomain = binDomain*(1/endTime);
figure('name', 'Magnitude vs Frequency FFT results - Linear', 'units', ...
    'normalize', 'position', [0.5, 0, 0.5, 0.5])
plot(freqDomain, Yfft_mag)
xlabel('bins', 'FontSize', 22) % understand how to convert to Hz
ylabel('Amplitude', 'FontSize', 22) % find out units of amplitude
xlim([0, freqDomain(end)/2])
set(gca, 'FontSize', 20)

```

accelerationFunction\_v5.m

```

function ydot = accelerationFunction_v5(y,t)

global g Me Ms r omega k L T theta

fsum2=-8*(k*sind(theta)*y(1)*sind(theta)...
    + T/L*cosd(theta)*y(1)*cosd(theta));

ydot1 = y(2);
ydot2 = (1/Ms)*fsum2-g+(Me/Ms)*r*omega^2*sin(omega*t);

ydot = [ydot1;ydot2];

end

```

## Appendix A.3: Natural Frequency Parameter Analysis

### NatrualFrequencyParameterAnalysis.m

```
% Single VVValtr Strut Vibration
% Natural Frequency Parameter Analysis
% Linear Model

clear all
close all

% Motor Frequency
omega = 2 * pi() * 12000 / 60; % rad/s
drivingFreq = omega/(2 * pi()); % Hz

% -----
% DEFAULT CALCULATIONS

% Input parameters
Ms = 0.0572; % Kg
k = 0.19 * 175.196945; % N/m
l0 = 2.47 * 0.0254; % m
lx = 3 * 0.0254; % m
F0 = 0.4 * 4.45; % N * NO INITIAL TENSION DATA FOR MCMaster SPRINGS*
h0 = 0.02; % m

% Dependent parameters
L=(lx^2+h0^2)^0.5; % m
T=k*(L - l0) + F0; % N
theta=atand(h0/lx); % deg

% Natrual frequency calculation
naturalFreq = sqrt(8*(k*sin(theta)^2+(T/L)*cos(theta)^2)/Ms)/(2*pi);

% -----
% VARIABLE MASS

% Variable range
MsRange = [0.05:0.001:0.5]; % Kg

naturalFreqMs = [];
for i = 1:length(MsRange)
    MsVar = MsRange(i);
    naturalFreqMs(i) = sqrt(8*(k*sind(theta)^2+...
        (T/L)*cosd(theta)^2)/MsVar)/(2*pi);
end

figure('name','VARIABLE MASS','units',...
    'normalized','position',[0,0,1,1])
subplot(2,2,1)
plot(MsRange,naturalFreqMs,'k')
set(gca, 'FontSize', 14)
xlabel('Strut Mass (Kg)','FontSize',16)
ylabel('Natural Frequency (Hz)','FontSize',16)
% ylim([0,60])
grid on
```



```

% -----
% VARIABLE SPRING RATE

% Variable range
kRange = [0:300]; % N/m

naturalFreqK = [];
for i = 1:length(kRange)
    kVar = kRange(i);
    TVar = kVar*(L - l0) + F0;
    naturalFreqK(i) = sqrt(8*(kVar*sind(theta)^2+...
        (TVar/L)*cosd(theta)^2)/Ms)/(2*pi);
end

% figure('name','VARIABLE SPRING RATE','units',...
%       'normalized','position',[0,0,1,1])
subplot(2,2,2)
plot(kRange,naturalFreqK,'k')
set(gca, 'FontSize', 14)
xlabel('Spring Rate (N/m)', 'FontSize', 16)
ylabel('Natural Frequency (Hz)', 'FontSize', 16)
% ylim([0,60])
grid on

% -----
% VARIABLE ANGLE

% Variable range
thetaRange = [0:0.1:90]; % deg

naturalFreqTheta = [];
for i = 1:length(thetaRange)
    thetaVar = thetaRange(i);
    naturalFreqTheta(i) = sqrt(8*(k*sind(thetaVar)^2+...
        (T/L)*cosd(thetaVar)^2)/Ms)/(2*pi);
end

% figure('name','VARIABLE ANGLE','units',...
%       'normalized','position',[0,0,1,1])
subplot(2,2,3)
plot(thetaRange,naturalFreqTheta,'k')
set(gca, 'FontSize', 14)
xlabel('Spring Angle at y=0 (deg)', 'FontSize', 16)
ylabel('Natural Frequency (Hz)', 'FontSize', 16)
xlim([0,90])
% ylim([0,60])
grid on

% -----
% VARIABLE STRECHED LENGTH

% Variable range
LRange = [10:0.001:0.25]; % m

naturalFreqL = [];
for i = 1:length(LRange)
    LVar = LRange(i);
    TVar = k*(LVar - l0) + F0;

```

```

        naturalFreqL(i) = sqrt(8*(k*sind(theta)^2+...
            (TVar/LVar)*cosd(theta)^2)/Ms)/(2*pi);
end

% figure('name','VARIABLE STRECHED LENGTH','units',...
%       'normalized','position',[0,0,1,1])
subplot(2,2,4)
plot(LRange,naturalFreqL,'k')
set(gca, 'FontSize', 14)
xlabel('Stretched Spring Length at y=0 (m)','FontSize',16)
ylabel('Natural Frequency (Hz)','FontSize',16)
xlim([10,0.25])
% ylim([0,60])
grid on

% -----
% VARIABLE INITIAL TENSION

% Variable range
F0Range = [0:0.01:1]; % N

naturalFreqF0 = [];
for i = 1:length(F0Range)
    F0Var = F0Range(i);
    TVar = k*(L - l0) + F0Var;
    naturalFreqF0(i) = sqrt(8*(k*sin(theta)^2+...
        (TVar/L)*cos(theta)^2)/Ms)/(2*pi);
end

% figure('name','VARIABLE INITIAL TENSION','units',...
%       'normalized','position',[0,0,1,1])
% subplot(3,2,5)
% plot(F0Range,naturalFreqF0,'k')
% set(gca, 'FontSize', 14)
% xlabel('Spring Tension (N)','FontSize',16)
% ylabel('Natural Frequency (Hz)','FontSize',16)
% % ylim([0,60])
% grid on

```

## Appendix A.4: Experimental Data Frequency Analysis MATLAB Code

### ExpFreqAnalysis.m

```
% Experimental Vibration Frequency Analysis

% NOTES:
% - SMOOTH ALL DATA AT BEGINNING SINCE MOST ACCURATE AMP DATA CAN BE
%   CALCULATED WITH IT, GIVEN PROPER ORDER AND WINDOW SIZE VALUES ARE
%   USED, AND IT DOESN'T EFFECT CALCULATED FREQUENCY

clc
clear all
close all

% -----

% PARAMETER SETTINGS
runtime = 30.001; % s
acclRange = 16; % +/-[2,4,8,16] g
gyroRange = 250; % +/-[250,500,1000,2000] dps
ststStartTime = 16; % observed start time for st-st in s

% -----

% LOAD TEST DATA AS ARRAY
data = load('test_d022618_t0248am_s130.txt'); % SINE WAVE BASED ON THIS
% data = load('test_d022618_t0248am_s130.txt');
% sp40_t30 = csvread('sp40_t30.csv');

% ISOLATE DOF
ax = data(:,1);
ay = data(:,2);
az = data(:,3);
% gx = data(:,1);
% gy = data(:,2);
% gz = data(:,3);

% CONVERT DOF VECTORS
ax = ax .* (acclRange/32768);
ay = ay .* (acclRange/32768);
az = az .* (acclRange/32768);
% gx = gx .* (gyroRange/32768);
% gy = gy .* (gyroRange/32768);
% gz = gz .* (gyroRange/32768);

% ADJUST ZERO REFERENCE FOR CALIBRATION
ax = ax - ax(1);
ay = ay - ay(1);
az = az - az(1);
% gx = gx - gx(1);
% gy = gy - gy(1);
% gz = gz - gz(1);

% -----

% DEPENDENT PARAMETERS
```

```

samples = length(ax(:,1));
deltat = runtime/samples;
t = 0:deltat:runtime-deltat;
rate = samples/runtime;
ststStartSample = ceil(ststStartTime*rate); % start sample for st-st in s

% -----

% FFT
ayFFT = fft(ay(ststStartSample:end)); % FFT of steady state region
ayFFT = abs(ayFFT); % convert FFT to magnitude spectrum
ayFFT = 2 .* ayFFT ./ length(ayFFT); % scale FFT to amplitude units
freqDomain = (0:length(ayFFT)-1) .* rate ./ length(ayFFT);

% plot(ay(ststStartSample:end));
% plot(ayFFT);

% DOMINANT SINE WAVE
[ayDomAmp,ayDomBin] = max(ayFFT);
ayDomFreq = freqDomain(ayDomBin);
disp(freqDomain(ayDomBin));
% ayDomWave = ayDomAmp * sin(2 * pi() * ayDomFreq .* t);
ayDomWave = max(ay) * sin(2 * pi() * ayDomFreq .* t);

% -----

% SMOOTHED WAVE DATA
% **larger window will cause more smoothing but greater amplitude decrease
axSmth = sgolayfilt(ax,3,7);
aySmth = sgolayfilt(ay,3,7);
azSmth = sgolayfilt(az,3,7);

% AVE SMOOTHED AMPLITUDE & FREQUENCY
peaks = findpeaks(aySmth((ststStartSample:end)));
peaks = peaks(peaks > 0);
aySmthAmp = mean(peaks);
aySmthFreq = length(peaks) / (runtime - deltat - ststStartTime);
disp(aySmthFreq);

% temp testing of fft on smoothed data to find freq
aySmthFFT = fft(aySmth(ststStartSample:end));
aySmthFFT = abs(aySmthFFT);
aySmthFFT = 2 .* aySmthFFT ./ length(aySmthFFT);
freqDomainSmth = (0:length(aySmthFFT)-1) .* rate ./ length(aySmthFFT);
[aySmthDomAmp,aySmthDomBin] = max(aySmthFFT);
aySmthDomFreq = freqDomainSmth(aySmthDomBin);
disp(freqDomainSmth(aySmthDomBin));

% -----

% PLOT FFT
figure('name','FFT Acceleration: y-axis','units','normalized',...
'position',[0,0,1,1])
plot(freqDomain,ayFFT)
xlim([0,rate/2])

% PLOT ACCL GRAPHS
figure('name','Acceleration Experimental Data','units','normalized',...

```

```

    'position',[0,0,1,1])

subplot(3,1,1)
plot(t,ax,'k');
hold on
% plot(t,axSmth,'k');
xlim([0,30.5])
ylim([-20,20])
xlabel('Time (s)','FontSize',16)
ylabel('Amplitude: x-axis (g)','FontSize',18)
set(gca, 'FontSize', 16)
grid on

subplot(3,1,2)
plot(t,ay,'k');
hold on
% plot(t,aySmth,'k');
% plot(t(ststStartSample:end),ayDomWave(ststStartSample:end),'--');
xlim([0,30.5])
ylim([-20,20])
xlabel('Time (s)','FontSize',16)
ylabel('Amplitude: y-axis (g)','FontSize',18)
set(gca, 'FontSize', 16)
grid on

subplot(3,1,3)
plot(t,az,'k');
hold on
% plot(t,azSmth,'k');
xlim([0,30.5])
ylim([-20,20])
xlabel('Time (s)','FontSize',16)
ylabel('Amplitude: z-axis (g)','FontSize',18)
set(gca, 'FontSize', 16)
grid on

figure('name','Y-axis Close Up Acceleration','units','normalized',...
    'position',[0,0,0.6,0.6])
plot(t,ay,'k');
xlim([20,21])
ylim([-20,20])
xlabel('Time (s)','FontSize',16)
ylabel('Amplitude: y-axis (g)','FontSize',18)
set(gca, 'FontSize', 16)
grid on

```

get\_freq\_exp.m

```

function freq_exp = get_freq_exp(data, runTime)
% This function determines the frequency of experimental sine wave data.
% Only works for simple waves.
% NOTE: Only enter range of data after oscillation starts and before
% amplitude becomes effected by noise.
% NOTE: Data must have at least five oscillations.
%
% file_var: name of variable loaded from ASCII file
% time_col: column in file_var containing time data

```

```

% data_col: column in file_var containing desired position data
% start_time: start time for peak count
% end_time: end time for peak count

first_peak = 1;
while data(first_peak + 1) <= data(first_peak)
    first_peak = first_peak + 1;
end
while data(first_peak + 1) >= data(first_peak)
    first_peak = first_peak + 1;
end

last_peak = length(data);
while data(last_peak - 1) <= data(last_peak)
    last_peak = last_peak - 1;
end
while data(last_peak - 1) >= data(last_peak)
    last_peak = last_peak - 1;
end

peak_count = 0; % number of peaks observed initialized to 0
increasing = 0; % initialize increasing as false

% Last peak is counted, first peak is not
for i = first_peak:last_peak + 1
    % check if function is increasing
    if increasing == 1
        % check if sample position value decreased
        if data(i) < data(i-1)
            % add to peak count
            peak_count = peak_count + 1;
            increasing = 0; % set increasing as false
        end
    elseif increasing == 0
        % check if sample position value increased
        if data(i) > data(i-1)
            increasing = 1; % set increasing as true
        end
    end
end

sRate = length(data)/runtime;

%calculate average frequency
freq_exp = (peak_count / (last_peak - first_peak)) * sRate;
end

```

## Appendix A.5: Experimental Data File Separator

expDataSplitter.m

```
% Data File Splitter
% Only works with .txt files

clear all

delimiter = 999999999;
startTimeCol = 1;
endTimeCol = 2;
speedValueCol = 3;

dataAllFileName = 'test_d022618_t0248am_s121_s249.txt';
dataAll = load(dataAllFileName);

[path,dataAllFileName,extension] =
fileparts(dataAllFileName); %#ok<ASGLU>
clear path extension

if exist(dataAllFileName) ~= 7
    mkdir(dataAllFileName)
end

c = 1;
nameChanged = false;
while nameChanged == false
    c = c + 1;
    if dataAllFileName(c:c+1) == '_s'
        fileName = dataAllFileName(1:c+1);
        nameChanged = true;
    end
end

prevTestDlmRow = 1;
for i = 1:length(dataAll)
    if dataAll(i,:) == [delimiter,delimiter,delimiter]
        testSpeed = dataAll(i-1,3);
        fileNameS = char(fileName+string(testSpeed));
        dlmwrite(fileNameS,dataAll(prevTestDlmRow:i-1,:))
        movefile(fileNameS,dataAllFileName)
        prevTestDlmRow = i+1;
    end
end
```

## Appendix A.6: Experimental Frequency Response Plot Script

frequencyResponse.m

```
% Frequency Response Plot

clear all
close all

maxMotorSpeed = 1300; % RPM

massFileFolder1 = 'test_d022518_t1223am_s15_s121';
minExpFreq1 = 15; % Hz
maxExpFreq1 = 121; % Hz

c = 1;
nameChanged = false;
while nameChanged == false
    c = c + 1;
    if massFileFolder1(c:c+1) == '_s'
        folderName1 = massFileFolder1(1:c+1);
        nameChanged = true;
    end
end

massFileFolder2 = 'test_d022618_t0248am_s121_s249';
minExpFreq2 = 122; % Hz
maxExpFreq2 = 249; % Hz

c = 1;
nameChanged = false;
while nameChanged == false
    c = c + 1;
    if massFileFolder2(c:c+1) == '_s'
        folderName2 = massFileFolder2(1:c+1);
        nameChanged = true;
    end
end

freqResp = zeros(maxExpFreq2-minExpFreq1+1,4);
i = 1;

for s = minExpFreq1:maxExpFreq1
    fileName = string('/') + string(massFileFolder1) + '/' + ...
        string(folderName1) + string(s);
    [axAmp, axFreq, ayAmp, ayFreq, azAmp, azFreq] ...
        = getAmpStSt(fileName, 30.001, 16, 28);
    %     freqResp(i,1) = (maxMotorSpeed/60) * (s/255);
    freqResp(i,1) = s;
    freqResp(i,2:7) = [axAmp, axFreq, ayAmp, ayFreq, azAmp, azFreq];
    i = i + 1;
end

for s = minExpFreq2:maxExpFreq2
    fileName = string('/') + string(massFileFolder2) + '/' + ...
        string(folderName2) + string(s);
    [axAmp, axFreq, ayAmp, ayFreq, azAmp, azFreq] ...
```



```

        = getAmpStSt(fileName,30.001,16,28);
%     freqResp(i,1) = (maxMotorSpeed/60) * (s/255);
    freqResp(i,1) = s;
    freqResp(i,2:7) = [axAmp,axFreq,ayAmp,ayFreq,azAmp,azFreq];
    i = i + 1;
end

figure('name','Y-axis Frequency REsponce','units','normalized',...
    'position',[0,0,1,1])
subplot(3,1,1)
plot(freqResp(:,1),freqResp(:,2),'k');
% hold on
% plot(freqResp(:,1),freqResp(:,5),'--k');
xlabel('Frequency (numerical input value)','FontSize',18)
ylabel('Amplitude: x-axis (g)','FontSize',18)
ylim([0,20])
set(gca, 'FontSize', 16)
grid on
subplot(3,1,2)
plot(freqResp(:,1),freqResp(:,4),'k');
% hold on
% plot(freqResp(:,1),freqResp(:,5),'--k');
xlabel('Frequency (numerical input value)','FontSize',18)
ylabel('Amplitude: y-axis (g)','FontSize',18)
ylim([0,20])
set(gca, 'FontSize', 16)
grid on
subplot(3,1,3)
plot(freqResp(:,1),freqResp(:,6),'k');
% hold on
% plot(freqResp(:,1),freqResp(:,5),'--k');
xlabel('Frequency (numerical input value)','FontSize',18)
ylabel('Amplitude: z-axis (g)','FontSize',18)
ylim([0,20])
set(gca, 'FontSize', 16)
grid on

```

## Appendix B: Eccentric weight design alternatives

